

Convolutional Autoencoders, Clustering, and POD for Low-dimensional Parametrization of Navier-Stokes Equations

Yongho Kim^{*,†} Jan Heiland^{*,†}

^{*}Max Planck Institute for Dynamics of Complex Technical Systems, Magdeburg, Germany
[†]Department of Mathematics, Otto von Guericke University Magdeburg, Magdeburg, Germany
 Email: ykim@mpi-magdeburg.mpg.de, ORCID: [0000-0003-4181-7968](https://orcid.org/0000-0003-4181-7968)
 Email: heiland@mpi-magdeburg.mpg.de, ORCID: [0000-0003-0228-8522](https://orcid.org/0000-0003-0228-8522)

Abstract: Simulations of large-scale dynamical systems require expensive computations. Low-dimensional parametrization of high-dimensional states such as Proper Orthogonal Decomposition (POD) can be a solution to lessen the burdens by providing a certain compromise between accuracy and model complexity. However, for really low-dimensional parametrizations (for example for controller design) linear methods like the POD come to their natural limits so that nonlinear approaches will be the methods of choice. In this work we propose a convolutional autoencoder (CAE) consisting of a nonlinear encoder and an affine linear decoder and consider combinations with k-means clustering for improved encoding performance. The proposed set of methods is compared to the standard POD approach in two cylinder-wake scenarios modeled by the incompressible Navier-Stokes equations.

Keywords: convolutional autoencoders, clustering, linear parameter varying (LPV) systems, model order reduction, incompressible flows.

AMS subject classifications: MSC1, MSC2, MSC3

Novelty statement:

- Convolutional autoencoders (CAEs) that handle FEM data for low-dimensional parametrization.
- Combination of encoders and decoders with clustering techniques for improved performance.
- Thorough demonstration of the capabilities of CAEs with clustering in comparison with POD in two cylinder-wake simulation scenarios.

1 Introduction

Accurate *Finite Element Method* (FEM) discretizations of fluid flow easily lead to dynamical systems with millions of degrees of freedom. This poses a computational challenge to simulations and, due to the involved nonlinearities, even more to computer-aided controller design based on these models.

The core idea and the promise of model order reduction techniques is the identification and exploitation of lower-dimensional coordinates that can well represent or approximate the dynamics of a generally high-dimensional systems. For example, *projection methods* like the successful method of *Proper Orthogonal Decomposition* (POD) base on linear projections onto subspaces that are designed to encode the most relevant dynamics of the system. These methods can efficiently reduce the dimension of the state space of a given dynamical systems and lead to significant savings of memory and computational requirements in simulations. However, linear methods are naturally limited in their accuracy for a given number of degrees of freedom as expressed by the *Kolmogorov n-width*, see e.g., [20].

Accordingly, if a very low-dimensional parametrization of still satisfactory accuracy is wanted, one may need to resort to nonlinear approaches; cp. [12, 18, 21].

Thus, in view of controller design where a low dimension is weighted higher than the actual accuracy, we consider methods to approximate and parametrize the states on a low-dimensional manifold by possibly non-linear maps.

Parametrization refers to representing the states of a given system in different coordinates, approximation means that this representation is designed to trade in accuracy for maximal low-dimensionality of the parametrizing coordinates. By *encoding* we will refer to the (computation of) reduced and parametrized representation of a state, whereas *decoding* or *reconstruction* describes the computation of the state in the actual coordinates from the parametrized representation. The according mechanisms or algorithms are referred to as *encoder* or *decoder*.

The method of POD, thus, can be seen as an encoder/decoder based on linear projections. As mentioned above, linear methods are limited so that nonlinear methods such as general *autoencoder* (AE) methods have been emerging as an alternative or an enhancement to POD [8].

An *autoencoder* (see e.g., [11, Ch. 14]) often refers to a *neural network* that is designed to efficiently encode data and that is trained by just considering the data itself. The underlying network architecture can be problem specific and contain several hidden layers. Nonlinearity in the encoding and decoding possibly arises from using activation function. Based on these principles, many types of autoencoders such as sparse autoencoders, denoising autoencoders, contractive autoencoders, and convolutional autoencoders have been developed. (see e.g., [3])

With the increasing availability of computing facilities and toolboxes for design and training of neural networks, since well over a decade, autoencoders have been considered as alternatives in the field of model order reduction. A recent example considers a modified nonlinear autoencoder that approximates the elements of the coefficient matrices of a linearized two-link planar robot manipulator; see [16]. Other examples target the solution of convection-dominated problems through deep convolutional autoencoders; see, e.g., [18])

With PDEs as the underlying model, the variants of autoencoders relying on so-called *Convolutional Neural Networks* (CNNs) [17] seem to be particularly useful as indicated by several attempts to use CNNs to solve PDEs; see e.g., [9, 14, 24] for current works. The realization of the linear part of the propagation from one layer to another as a convolution drastically reduces the parameters of the network by enforcing *sparse connectivity*, meaning that over the layers every variable is related to only a limited number of other variables. Moreover, the accompanying operation of *pooling*, that coalesces several neighboring variables into one, reduces the variable dimension in every layer. In classical FEM approaches, sparse connectivity is a major performance criterion and generally achieved by considering basis functions with local support whereas the *pooling* can be related to multiscale approaches.

Once a very low-dimensional code of a state has been derived, it is the task of the decoder to reconstruct the high-dimensional state from the code. Intuitively spoken, the design of the decoder becomes increasingly complex the higher variations in the output space it should reproduce. Accordingly, we suppose that clustering in the reduced order coordinates will well separate the state space so that separate individual decoders then only need to cover a certain range in the overall variety; see [13] for an example implementation.

Clustering algorithms are used to distinguish data and divide a given dataset into certain subsets without the use of labels, i.e. without knowing characteristics of the subset in advance; see, e.g.,

[22] for clustering in general and [23] for a discussion of the most popular clustering algorithm – the *k-means clustering* – that iteratively identifies a predefined number of clusters in a data set based on distance measures. Moreover, clustering algorithms well integrate with neural networks, the more that clustering becomes easier in low data dimensions like in low-dimensional feature spaces; see e.g., [2, 7, 19].

Since clustering is not a smooth operation, such an approach has not been attempted in dynamical systems until recently. Nonetheless, it has been observed that dimensionality reduction techniques with clustering improve retrieval performance and reduce computational costs by individually processing subsets of a large-scale dataset, e.g., in text retrieval systems; see [10].

In this work, with the focus on identifying very low-dimensional parametrizations of states (as opposed to low-dimensional dynamical models) the nonsmoothness is not an issue so that we can directly adopt clustering in the numerical studies.

This paper is organized as follows: In Section 2, we introduce the incompressible Navier-Stokes equation which will be our FEM model under consideration. In Section 3, we define low-dimensional parametrization methods. In Section 4, we discuss how to build each reduced order model using considered methods respectively. In Section 5, we show the results of the reconstruction errors of the methods and evaluate the reduced order models based on their residuals. In Section 6, we sum up the paper, discuss limitations, and lay out potential research directions for future work.

2 Incompressible Navier-Stokes Equations

We consider the dynamical system of spatially discretized incompressible Navier-Stokes equations

$$\mathbf{M}\dot{\mathbf{v}}(t) + \mathbf{N}(\mathbf{v}(t))\mathbf{v}(t) + \mathbf{A}\mathbf{v}(t) - \mathbf{J}^\top \mathbf{p}(t) = \mathbf{f}(t) \quad (1a)$$

$$\mathbf{J}\mathbf{v}(t) = 0, \quad (1b)$$

where for time $t > 0$, $\mathbf{v}(t) \in \mathbb{R}^{n_v}$ and $\mathbf{p}(t) \in \mathbb{R}^{n_p}$ denote the states of the velocity and the pressure respectively on the FEM mesh, and where $\mathbf{M} \in \mathbb{R}^{n_v \times n_v}$ is the mass matrix, where $\mathbf{A} \in \mathbb{R}^{n_v \times n_v}$ models the diffusion, where $\mathbf{N}: \mathbb{R}^{n_v} \rightarrow \mathbb{R}^{n_v \times n_v}$ represents the discretized convection, and where $\mathbf{J} \in \mathbb{R}^{n_p \times n_v}$ and \mathbf{J}^\top denote the discrete divergence and gradient, respectively; see [4] for technical details and example discretizations.

In what follows, we will drop the time dependency in the variables \mathbf{v} (and later also ρ and $\tilde{\mathbf{v}}$ which will denote the code and the reconstruction).

As it is common practice at least for theoretical considerations, the system (1) can be expressed as an ordinary differential equation. Here, we will use the ODE formulation to avoid technical difficulties with treating the p variable in numerical schemes (cp. [1]) and to be directly adaptable to other ODE models.

We briefly lay out, how the ODE formulation of the incompressible Navier-Stokes equations is obtained. Under the reasonable assumption that \mathbf{J} is of full rank and \mathbf{M} is invertible and symmetric positive definite, by means of the equation $\mathbf{p} = \mathbf{S}^{-1}\mathbf{J}\mathbf{M}^{-1}(\mathbf{N}(\mathbf{v})\mathbf{v} + \mathbf{A}\mathbf{v} - \mathbf{f})$ where $\mathbf{S} = \mathbf{J}\mathbf{M}^{-1}\mathbf{J}^\top$, we can eliminate \mathbf{p} from (1) and obtain

$$\mathbf{M}\dot{\mathbf{v}} + (\mathbf{I} - \mathbf{J}^\top \mathbf{S}^{-1} \mathbf{J} \mathbf{M}^{-1})(\mathbf{N}(\mathbf{v})\mathbf{v} + \mathbf{A}\mathbf{v} - \mathbf{f}) = 0.$$

With the projector $\Pi := \mathbf{I} - \mathbf{M}^{-1}\mathbf{J}^\top \mathbf{S}^{-1} \mathbf{J}$ and having confirmed that the solution v satisfies $v = \Pi v$, we can state that for the computation of v , system (1) can be replaced by

$$\mathbf{M}\dot{\mathbf{v}} + \Pi^\top (\mathbf{N}(\mathbf{v})\mathbf{v} + \mathbf{A}\mathbf{v} - \mathbf{f}) = 0. \quad (2)$$

In the next sections we will investigate how well the state \mathbf{v} can be encoded in a very low-dimensional code ρ with respect to several measures. Firstly, the standard reconstruction error

$$\|\mathbf{v}(t) - \tilde{\mathbf{v}}(t)\|_{\mathbf{M}}$$

that we measure in the so-called \mathbf{M} -norm that is induced by the mass matrix \mathbf{M} and that is discrete and consistent counterpart of the L^2 Sobolev norm associated with the underlying model problem. Secondly, the reconstruction with respect to the resulting convection is considered by measuring

$$\|\mathbf{N}(\tilde{\mathbf{v}}(t))\mathbf{v}(t) - \mathbf{N}(\mathbf{v}(t))\mathbf{v}(t)\|_{\mathbf{M}^{-1}},$$

where the \mathbf{M}^{-1} norm is chosen to account for the FEM context in which $\mathbf{N}(\mathbf{v}(t))\mathbf{v}(t)$ is a functional.

Finally, in view of possibly providing related surrogate low-order dynamical models, we will report on the residuals at the data points.

3 Low-dimensional Parametrization

In this section, we consider a number of possibly nonlinear methods for encoding and decoding with a focus on very low-dimensional parametrizations and with the standard method POD as a benchmark.

As introduced above, we will use \mathbf{V} to denote the velocity with values in \mathbb{R}^{n_v} , $\boldsymbol{\rho}$ to denote the code with values in \mathbb{R}^{n_ρ} , and $\tilde{\mathbf{v}}$ to denote the reconstruction of the velocity from the code. The considered approaches are as follows:

3.1 Proper Orthogonal Decomposition (POD)

The method of POD [5] is readily interpreted as an autoencoder with

- (1) a *linear* encoder defined as

$$\boldsymbol{\rho} = \mathbf{V}^\top \mathbf{v}$$

- (2) and a *linear* decoder

$$\tilde{\mathbf{v}} = \mathbf{V}\boldsymbol{\rho},$$

where $\mathbf{V} \in \mathbb{R}^{n_v \times n_\rho}$ is a POD basis that is, typically, computed as the n_ρ leading singular vectors of a matrix of snapshots of the variable \mathbf{v} .

3.2 Convolutional Neural Network (CNN)

In order to apply standard convolutional approaches, the input data needs to be available on a tensorized grid, i.e., a grid of rectangles with no hanging nodes and that are aligned with the coordinate axes; see [13, Fig. 3 and 4] for an illustration of this interpolation. To achieve that make use of corresponding interpolation matrix \mathbf{I}_c such that the CNN input $\mathbf{v}_{\text{CNN}}(t)$ can be generated by the linear transformation $\mathbf{v}_{\text{CNN}}(t) = \mathbf{I}_c \mathbf{v}(t)$. We consider the CNN architecture introduced as introduced in [12] that makes use of POD modes for the reconstruction. Thus, the CNN is defined as a model consisting of

- (1) a *nonlinear convolutional* encoder μ :

$$\boldsymbol{\rho} = \mu(\mathbf{v}_{\text{CNN}})$$

- (2) and a *linear* decoder

$$\tilde{\mathbf{v}} = \phi(\boldsymbol{\rho}) = \mathbf{V}(\mathbf{W}\boldsymbol{\rho}),$$

where $\mathbf{v}_{\text{CNN}} \in \mathbb{R}^{2 \times w \times h}$ is a CNN input, $\mathbf{V} \in \mathbb{R}^{n_v \times r}$ is a POD basis with r modes, and $\mathbf{W} \in \mathbb{R}^{r \times n_\rho}$ is a trainable matrix. The feedforward network of the decoder μ in (1) is concretely described as follows:

$$\mathbf{u}^{(m)} = \mathbf{a}(\mathbf{F}^{(m)}(\mathbf{u}^{(m-1)})), \quad \mathbf{u}^{(0)} = \mathbf{v}_{\text{CNN}}, \quad m = 1, \dots, M-1,$$

$$\mathbf{u}^{(M)} = \mathbf{F}^{(M)}(\mathbf{u}^{(M-1)}),$$

$$\boldsymbol{\rho} = \mathbf{U}\bar{\mathbf{u}}^{(M)} + \boldsymbol{\beta}, \quad \mathbf{U} \in \mathbb{R}^{n_\rho \times n_u}, \quad \boldsymbol{\beta} \in \mathbb{R}^{n_\rho},$$

where \mathbf{a} is a nonlinear activation function, M is the number of convolutional layers, \mathbf{F} is a convolutional layer, $\bar{\mathbf{u}}^{(M)}$ is the vectorized $\mathbf{u}^{(M)}$, and n_u is the dimension of $\bar{\mathbf{u}}^{(M)}$.

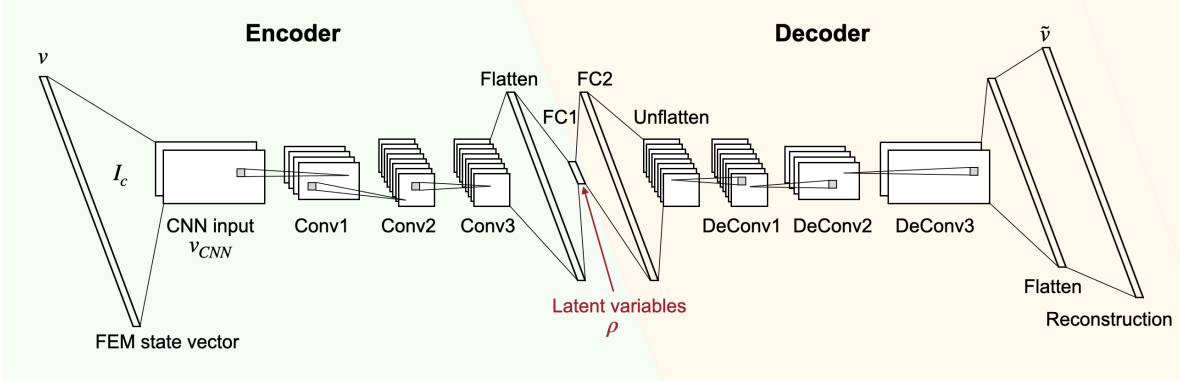


Figure 1: Convolutional Autoencoder for the reconstruction of FEM state vectors

3.3 Convolutional Autoencoder (CAE)

Other than using POD modes for the reconstruction, we propose the use of so-called *transposed* convolutional layers without nonlinear activation and with an interpolation operator \mathbf{I}_p that interpolates the values from the tensorized grid back to the FEM grid. Thus, we can investigate the CNN properties for reconstruction while – as a composition of affine-linear operators – keeping the process affine-linear.

This proposed model, thus, consists of

- (1) a *nonlinear convolutional* encoder

$$\mu: \mathbf{v}_{\text{CNN}} \rightarrow \boldsymbol{\rho}$$

and

- (2) an *affine linear deconvolutional* decoder

$$\tilde{\mathbf{v}} = \phi(\boldsymbol{\rho}) = \mathbf{D}\boldsymbol{\rho} + \mathbf{b}$$

where $\mathbf{D} \in \mathbb{R}^{n_v \times n_\rho}$ is a matrix, and $\mathbf{b} \in \mathbb{R}^{n_v}$ is a vector.

In practice, the decoder $\phi: \boldsymbol{\rho} \rightarrow \tilde{\mathbf{v}}$ is realized via:

$$\begin{aligned} \bar{\mathbf{z}}^{(0)} &= \mathbf{U}\boldsymbol{\rho} + \boldsymbol{\beta}, \quad \mathbf{U} \in \mathbb{R}^{n_u \times n_\rho}, \boldsymbol{\beta} \in \mathbb{R}^{n_u}, \\ \mathbf{z}^{(m)} &= \mathbf{G}^{(m)}(\mathbf{z}^{(m-1)}), \quad m = 1, \dots, M, \quad \text{with } \mathbf{z}^{(0)} \text{ as the unflattened } \bar{\mathbf{z}}^{(0)} \\ \tilde{\mathbf{v}} &= \mathbf{I}_p \bar{\mathbf{z}}^{(M)}, \quad \mathbf{I}_p \in \mathbb{R}^{n_z \times n_v}, \end{aligned}$$

where M is the number of layers, \mathbf{G} is a deconvolutional layer, $\bar{\mathbf{z}}^{(M)}$ is the vectorized $\mathbf{z}^{(M)}$, and n_z is the dimension of $\bar{\mathbf{z}}^{(M)}$. The architecture is shown in [Figure 1](#).

3.4 Clustered POD (cPOD)

As motivated in the introduction, the reconstruction performance can well be improved by using multiple decoders depending on clusters. Before we go for clustering with general autoencoders, we define a *clustered POD* (cPOD) as a model consisting of

- (1) a *linear* encoder

$$\boldsymbol{\rho} = \mathbf{V}^\top \mathbf{v},$$

Table 1: Description of the CNN-based models

–	CNN	CAE
#encoding layers	4 + fc	3 + fc
#convolution channels	(4, 8, 10, 12)	(4, 8, 8)
#decoding layers	fc + \mathbf{V}	fc + 3 + fc
#deconvolution channels	-	(8, 8, 4)

* fc: a fully connected layer, \mathbf{V} : a POD basis with r modes

(2a) a cluster selection algorithm

$$c: \boldsymbol{\rho}(t) \mapsto l \in \{1, 2, \dots, k\}, \quad (5)$$

(2b) and k linear decoders

$$\tilde{\mathbf{v}} = \mathbf{V}_l(\mathbf{V}_l^\top \mathbf{V})\boldsymbol{\rho},$$

where \mathbf{V} is a POD basis based on the whole data, where $\mathbf{V}_l \in \mathbb{R}^{n_v \times n_\rho}$ is a POD basis associated with the l -th cluster, $l = 1, 2, \dots, k$ and where k is the number of clusters. For setting up the model, we employ k -means clustering on the low-dimensional state vectors $\boldsymbol{\rho}$, classify the actual data \mathbf{v} accordingly and then compute POD bases for each cluster separately. Thus, during evaluation, a label $l \in \{1, \dots, k\}$ is extracted from the reduced state vector $\boldsymbol{\rho}(t)$ and a proper POD basis is selected for the given label. Note that clustering is *nonlinear* and *discontinuous* so the decoding becomes nonlinear and discontinuous as well.

3.5 Individual CAE (iCAE)

As another clustering approach, we adapt the individual CAE approach (iCAEs) that we proposed in [13] for CNNs with POD based reconstruction for the use of general CAEs as in Section 3.3. An iCAE model consists of

(1) a *nonlinear convolutional* encoder

$$\mu: \mathbf{v}_{\text{CNN}} \rightarrow \boldsymbol{\rho}$$

as in Section 3.3(1), of (2a) a clustering operation as in Section 3.4(2a) and

(2b) k *affine linear deconvolutional* decoders

$$\tilde{\mathbf{v}} = \phi_l(\boldsymbol{\rho}),$$

where ϕ_l is the l -th affine linear deconvolutional decoder trained by the l -th cluster. The encoder is continuous and differentiable. The decoding, on the other hand, is nonlinear and discontinuous. It is known that data compression can improve clustering accuracy. Since a CAE is trained in advance of training an iCAE, the pretrained encoder can be used without any extra training, and reduced low-dimensional states $\boldsymbol{\rho}$ can be used for k -means clustering. Thus, we train only k decoders based on k clusters while freezing the encoder parameters. In the inference, a reduced vector $\boldsymbol{\rho}$ and a label are yielded simultaneously once the encoder extracts a reduced state vector, and then a proper decoder is selected based on the label.

4 Low-order Parametrization of the State and the Models

In this section, we apply the aforementioned models of Section 3 to define low-dimensional LPV approximations of the incompressible Navier-Stokes equation in the ODE form of (2). Where applicable, i.e., where the decoding is linear, we lay out the affine-linear structure of the LPV approximation that

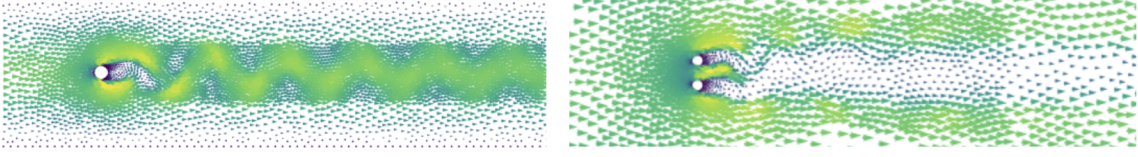


Figure 2: Two snapshots of developed velocity states: (left) a single cylinder case at $\text{Re}=40$ (right) a double cylinder case at $\text{Re}=50$

is naturally induced by the quadratic nature of the Navier-Stokes equations since $\mathbf{v} \mapsto \mathbf{N}(\mathbf{v})$ is linear; see also [12]. We note that we are mostly interested in low-dimensional parameterized approximations of the nonlinear term. Nonetheless, for the methods with a differentiable decoder, we also state the equations in the reduced order coordinates. In particular, as mentioned, the clustering methods lead to non-continuous reconstructions $\tilde{\mathbf{v}}$ so that $\dot{\tilde{\mathbf{v}}}$ might not be defined.

Numerical evaluations of the residuals for two test cases will be reported in Section 5.

1. For the **POD** encoder, the parametrization reads

$$\mathbf{M}\dot{\mathbf{v}} + \Pi^\top \left[\left(\sum_{i=1}^{n_\rho} \rho_i(\mathbf{v}) \mathbf{N}(\mathbf{w}_i) \right) \mathbf{v} + \mathbf{A}\mathbf{v} - \mathbf{f} \right] = 0$$

where $\boldsymbol{\rho}(\mathbf{v}) = \mathbf{V}^\top \mathbf{v}$, and \mathbf{w}_i is the i -th column vector of the POD basis \mathbf{V} as defined in Section 3.1. The model in the reduced coordinates reads

$$\hat{\mathbf{M}}\dot{\boldsymbol{\rho}} + \Pi^\top \left[\left(\sum_{i=1}^{n_\rho} \rho_i \hat{\mathbf{N}}(\mathbf{w}_i) \right) \boldsymbol{\rho} + \hat{\mathbf{A}}\boldsymbol{\rho} - \mathbf{f} \right] = 0, \quad (6)$$

where $\hat{\mathbf{M}} := \mathbf{M}\mathbf{V}$, $\hat{\mathbf{A}} := \mathbf{A}\mathbf{V}$, and $\hat{\mathbf{N}}(\cdot) := \mathbf{N}(\cdot)\mathbf{V}$. Further note that the standard POD reduced order model is obtained from (6) by a multiplication by \mathbf{V}^\top from the left.

2. For the **CNN** method, the parametrized equations read

$$\mathbf{M}\dot{\mathbf{v}} + \Pi^\top \left[\left(\sum_{i=1}^{n_\rho} \rho_i(\mathbf{v}) \mathbf{N}(\mathbf{w}_i) \right) \mathbf{v} + \mathbf{A}\mathbf{v} - \mathbf{f} \right] = 0$$

where $\boldsymbol{\rho}(\mathbf{v}) = \boldsymbol{\mu}(\mathbf{v})$, and \mathbf{w}_i is the i -th column vector of $\mathbf{V}\mathbf{W}$; see Section 3.2. The equations in the reduced coordinates are obtained by

$$\hat{\mathbf{M}}\dot{\boldsymbol{\rho}} + \Pi^\top \left[\left(\sum_{i=1}^{n_\rho} \rho_i \hat{\mathbf{N}}(\mathbf{w}_i) \right) \boldsymbol{\rho} + \hat{\mathbf{A}}\boldsymbol{\rho} - \mathbf{f} \right] = 0$$

where $\hat{\mathbf{M}} := \mathbf{M}\mathbf{V}\mathbf{W}$, $\hat{\mathbf{A}} := \mathbf{A}\mathbf{V}\mathbf{W}$, and $\hat{\mathbf{N}}(\cdot) := \mathbf{N}(\cdot)\mathbf{V}\mathbf{W}$.

3. For the **CAE** model, the parametrized equations read

$$\mathbf{M}\dot{\mathbf{v}} + \Pi^\top \left[\left(\mathbf{N}(\mathbf{b}) + \sum_{i=1}^{n_\rho} \rho_i(\mathbf{v}) \mathbf{N}(\mathbf{d}_i) \right) \mathbf{v} + \mathbf{A}\mathbf{v} - \mathbf{f} \right] = 0$$

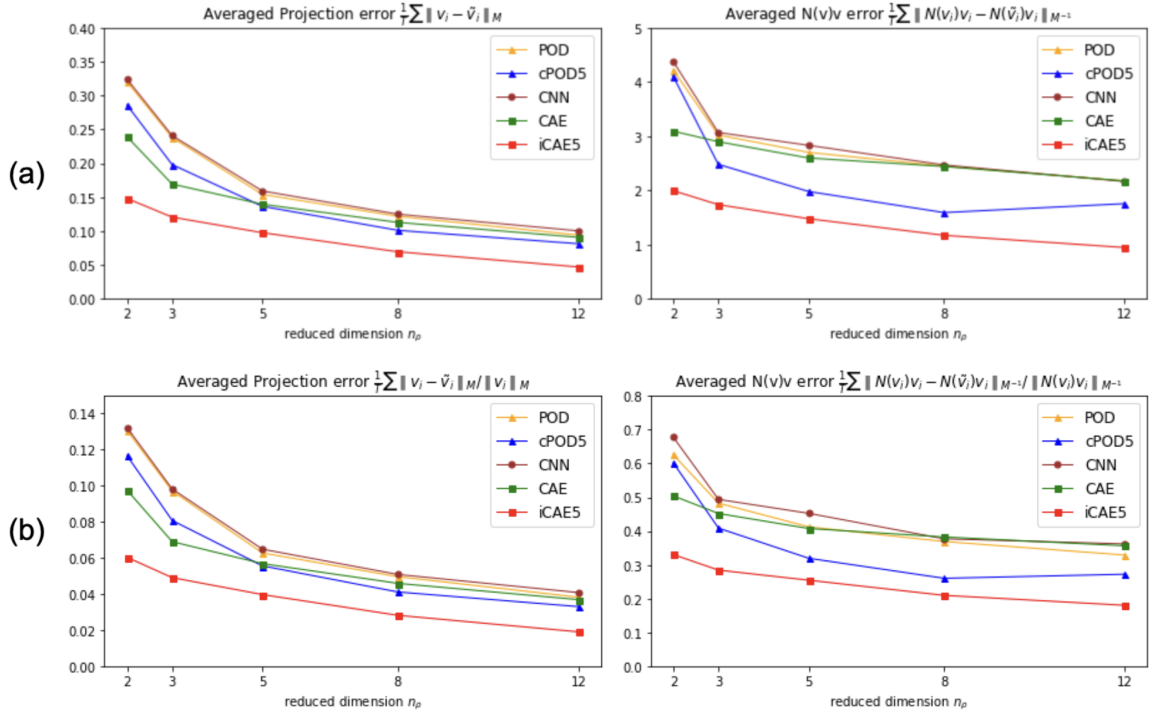


Figure 3: (a) Averaged reconstruction errors (b) Averaged relative errors for the single cylinder case (Section 5.1).

where $\boldsymbol{\rho}(\mathbf{v}) = \boldsymbol{\mu}(\mathbf{v})$ and \mathbf{b} is the bias of the decoder and \mathbf{d}_i is the i -th column vector of \mathbf{D} ; see Section 3.3. The equations in the reduced coordinates are obtained by

$$\hat{\mathbf{M}}\boldsymbol{\rho} + \Pi^\top \left[(\mathbf{N}(\mathbf{b}) + \sum_{i=1}^{n_\rho} \rho_i \mathbf{N}(\mathbf{d}_i)) (\mathbf{D}\boldsymbol{\rho} + \mathbf{b}) + \hat{\mathbf{A}}\boldsymbol{\rho} + \hat{\mathbf{f}} \right] = 0$$

where $\hat{\mathbf{M}} := \mathbf{M}\mathbf{D}$, $\hat{\mathbf{A}} := \mathbf{A}\mathbf{D}$, and $\hat{\mathbf{f}} := \mathbf{A}\mathbf{b} - \mathbf{f}$.

4. For the **cPOD** model, the parametrized equations read

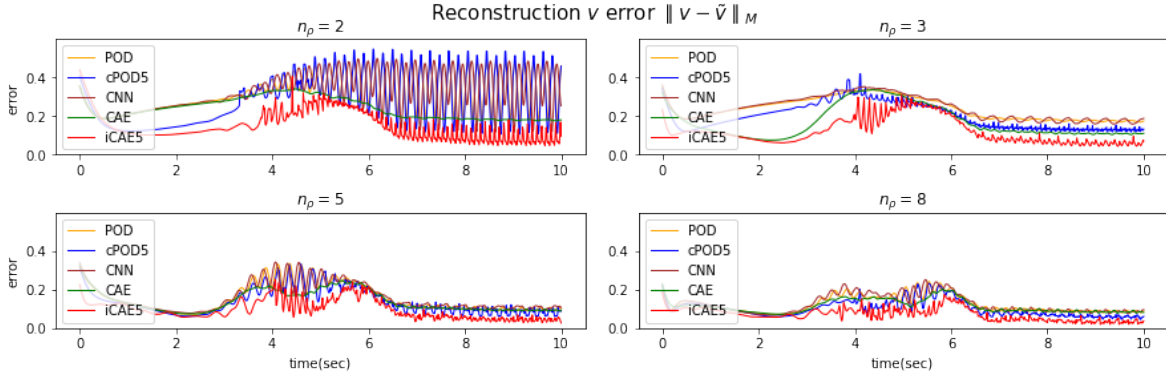
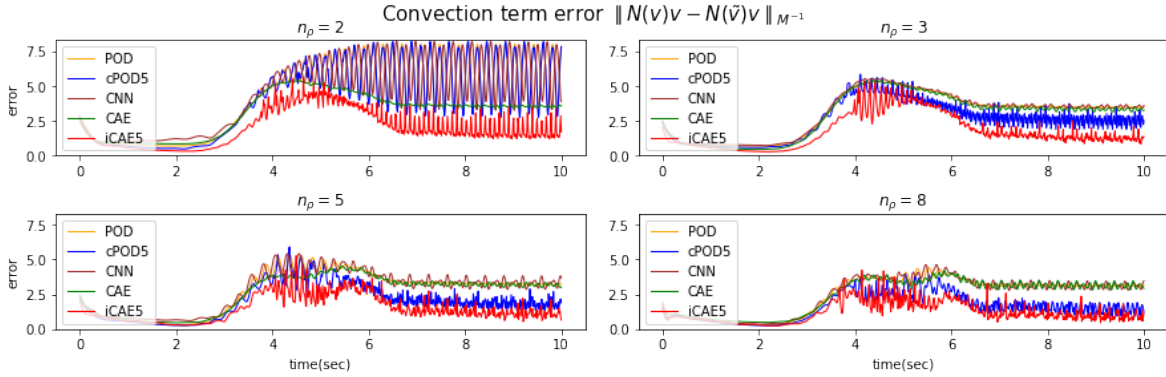
$$\mathbf{M}\dot{\mathbf{v}} + \Pi^\top \left[\left(\sum_{i=1}^{n_\rho} \rho_i(\mathbf{v}) \mathbf{N}(\mathbf{w}_i^l) \right) \mathbf{v} + \mathbf{A}\mathbf{v} - \mathbf{f} \right] = 0$$

where $\boldsymbol{\rho}(\mathbf{v}) = \mathbf{V}^\top \mathbf{v}$ and \mathbf{w}_i^l is the i -th column vector of the matrix $\mathbf{V}_l (\mathbf{V}_l^\top \mathbf{V})$ with the overall POD basis \mathbf{V} and the POD basis \mathbf{V}_l of the corresponding cluster; see Section 3.4.

5. For the **iCAE** model, the parametrized equations read

$$\mathbf{M}\dot{\mathbf{v}} + \Pi^\top \left[(\mathbf{N}(\mathbf{b}_l) + \sum_{i=1}^{n_\rho} \rho_i(\mathbf{v}) \mathbf{N}(\mathbf{d}_i^l)) \mathbf{v} + \mathbf{A}\mathbf{v} - \mathbf{f} \right] = 0$$

where $\boldsymbol{\rho}(\mathbf{v}) = \boldsymbol{\mu}(\mathbf{v})$, \mathbf{b}_l is the bias of the l -th decoder and \mathbf{d}_i^l is the i -th column vector of \mathbf{D}_l ; see Section 3.5.

Figure 4: Reconstruction error in $[0, 10]$ for the single cylinder case (Section 5.1).Figure 5: Convection error in $[0, 10]$ for the single cylinder case (Section 5.1).

As for the **iCAE** and **cPOD** models, we note that the dependence of $l = l(\boldsymbol{\rho})$ on $\boldsymbol{\rho}$ via the labelling algorithm (5) introduces a nonlinearity in the decoding. Nonetheless, as the $n_\rho \cdot k$ coefficients $\mathbf{N}(\mathbf{w}_i^l)$ or $\mathbf{N}(\mathbf{d}_i^l)$ can be precomputed, $i = 1, \dots, n_\rho$, $l = 1, \dots, k$, where k is the number of clusters, the inherent affine linear structure in the reduced order models can be exploited for efficient realizations in numerical simulations.

5 Numerical Examples

The cylinder wake is an established benchmark example that generates diverse flow patterns depending on simulation settings and the Reynolds number. In this section, we consider two-dimensional cylinder-wake phenomena observed behind a single cylinder and two cylinders respectively as shown in Figure 2. We investigate how the models generate reconstructed state vectors by using data including periodic wakes behind a single cylinder and data containing chaotic vortices behind two cylinders respectively. Moreover, the main topic of the work is to investigate very low-dimensional parametrization of incompressible flows so $n_\rho = 2, 3, 5, 8, 12$ are used.

The raw data, all routines and a script for reproducing the presented results are publicly available as described at the end of the manuscript in Section 7.

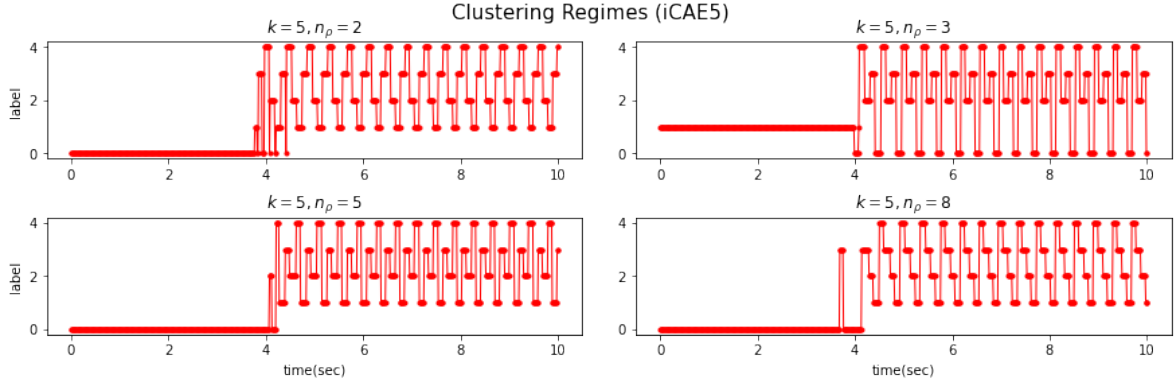


Figure 6: Prompt clustering reaction in $[0, 10]$ for the single cylinder case (Section 5.1).

For the evaluation of all experiments, we use the six evaluation metrics as follows:

- The averaged reconstruction error

$$\frac{1}{T} \sum_{i=1}^T \|\mathbf{v}_i - \tilde{\mathbf{v}}_i\|_{\mathbf{M}},$$

- the averaged relative error of reconstruction \mathbf{v}

$$\frac{1}{T} \sum_{i=1}^T \|\mathbf{v}_i - \tilde{\mathbf{v}}_i\|_{\mathbf{M}} / \|\mathbf{v}_i\|_{\mathbf{M}}$$

- the averaged convection term error,

$$\frac{1}{T} \sum_{i=1}^T \|\mathbf{N}(\mathbf{v}_i)\mathbf{v}_i - \mathbf{N}(\tilde{\mathbf{v}}_i)\mathbf{v}_i\|_{\mathbf{M}^{-1}},$$

- the averaged relative error of reconstruction $\mathbf{N}(\mathbf{v})\mathbf{v}$

$$\frac{1}{T} \sum_{i=1}^T \|\mathbf{N}(\mathbf{v}_i)\mathbf{v}_i - \mathbf{N}(\tilde{\mathbf{v}}_i)\mathbf{v}_i\|_{\mathbf{M}^{-1}} / \|\mathbf{N}(\mathbf{v}_i)\mathbf{v}_i\|_{\mathbf{M}^{-1}},$$

- the averaged residual

$$\frac{1}{T} \sum_{i=1}^T \|\Pi^\top[(\mathbf{N}(\tilde{\mathbf{v}})\tilde{\mathbf{v}} + \mathbf{A}\tilde{\mathbf{v}}) - (\mathbf{N}(\mathbf{v})\mathbf{v} + \mathbf{A}\mathbf{v})]\|_{\mathbf{M}^{-1}},$$

- and the averaged relative residual

$$\frac{1}{T} \sum_{i=1}^T \|\Pi^\top[(\mathbf{N}(\tilde{\mathbf{v}})\tilde{\mathbf{v}} + \mathbf{A}\tilde{\mathbf{v}}) - (\mathbf{N}(\mathbf{v})\mathbf{v} + \mathbf{A}\mathbf{v})]\|_{\mathbf{M}^{-1}} / \|\Pi^\top(\mathbf{N}(\mathbf{v})\mathbf{v} + \mathbf{A}\mathbf{v})\|_{\mathbf{M}^{-1}},$$

where $\|\mathbf{x}\|_{\mathbf{M}} = \sqrt{\mathbf{x}^\top \mathbf{M} \mathbf{x}}$, \mathbf{v}_i is a target velocity, $\tilde{\mathbf{v}}_i$ is a reconstructed velocity and T is the number of snapshots.

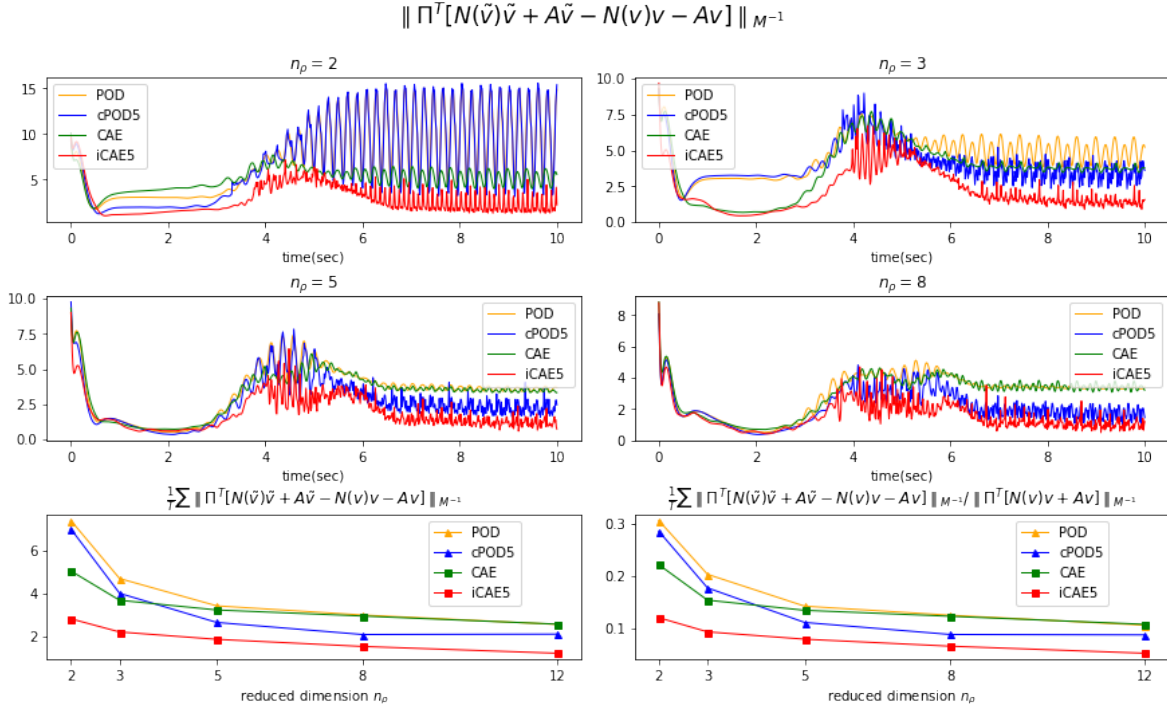


Figure 7: Error of $\Pi^\top[\mathbf{N}(\tilde{\mathbf{v}})\tilde{\mathbf{v}} + \mathbf{A}\tilde{\mathbf{v}} - \mathbf{N}(\mathbf{v})\mathbf{v} + \mathbf{A}\mathbf{v}]$ in $[0, 10]$ (Section 5.1).

5.1 Single Cylinder

As for the training, namely to set up the POD basis and to train the neural networks and the clustering algorithm, we use 400 equidistant snapshots of x and y directional velocities in $[0, 10]$. The snapshots were generated by a FEM simulation of Equation (1) for a cylinder wake with a Reynolds number of 40 starting at the somewhat nonphysical associated Stokes solution. All data points $\mathbf{v}(t) \in \mathbb{R}^{42764}$ (i.e., $n_v = 42764$) are spatially distributed in the domain $(0, 5) \times (0, 1)$. To feed the data into the convolutional neural networks, the CNN input data $\mathbf{v}_{\text{CNN}}(t) \in \mathbb{R}^{2 \times 47 \times 63}$ are generated by means of an interpolation matrix $\mathbf{I}_c \in \mathbb{R}^{42764 \times 5922}$ followed by a reshaping of the data vector into the 3D tensor. For the evaluation dataset, the same conditions were used to generate 800 snapshots on $[0, 10]$.

The parameters of the CNN/CAE models are listed in Table 1. Basically, the CNN model includes four convolutional layers and a fully connected layer in the encoder, and the decoder uses a linear transformation and a POD basis $\mathbf{V} \in \mathbb{R}^{42764 \times 15}$ (i.e., $r = 15$) to map the reduced parameters back to the original state space.

The encoder of the CAE contains three convolutional layers and a fully connected layer. The decoder conducts successively a fully connected layer, three deconvolutional layers, and a fully connected layer. In the encoder part, a nonlinear activation function *ELU* [6] is applied in each hidden layer of the encoders. For the clustering models, the number of clusters k is 5 and the considered clustering models are called cPOD5 and iCAE5 respectively.

In the training session of the networks, we use the ADAM optimizer [15] with a multistep learning rate scheduler and a batch size of 64. As a loss function, the mean square error is used. When the CAE is trained using \mathbf{v}_{CNN} data, an interpolation matrix \mathbf{I}_p satisfying $\mathbf{v} = \mathbf{I}_p \mathbf{v}_{\text{CNN}}$ is used to return to the states from the tensorized grid to the FEM mesh. Note that because of the rather rough tensorized grid, the two interpolations mean a major loss of details and that, in particular, $\mathbf{v} \neq \mathbf{I}_p \mathbf{I}_c \mathbf{v}$.

As the use of \mathbf{I}_p and \mathbf{I}_c means a significant loss of accuracy, one could try to rather learn these

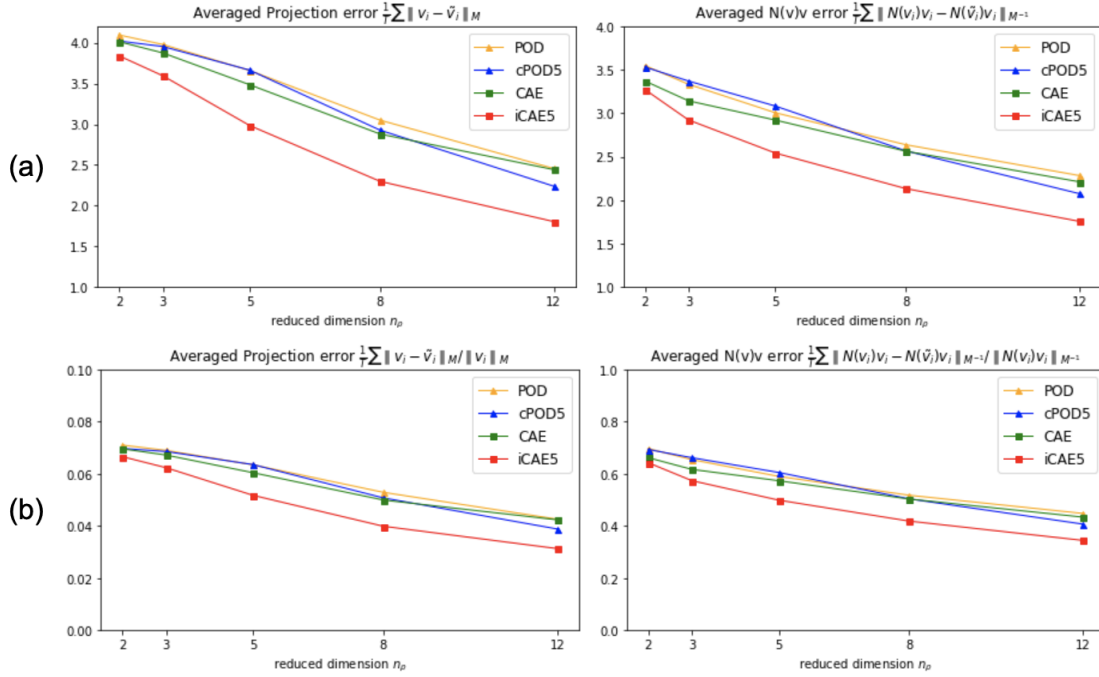


Figure 8: (a) Averaged reconstruction errors and (b) Averaged relative errors for the double cylinder case (Section 5.2).

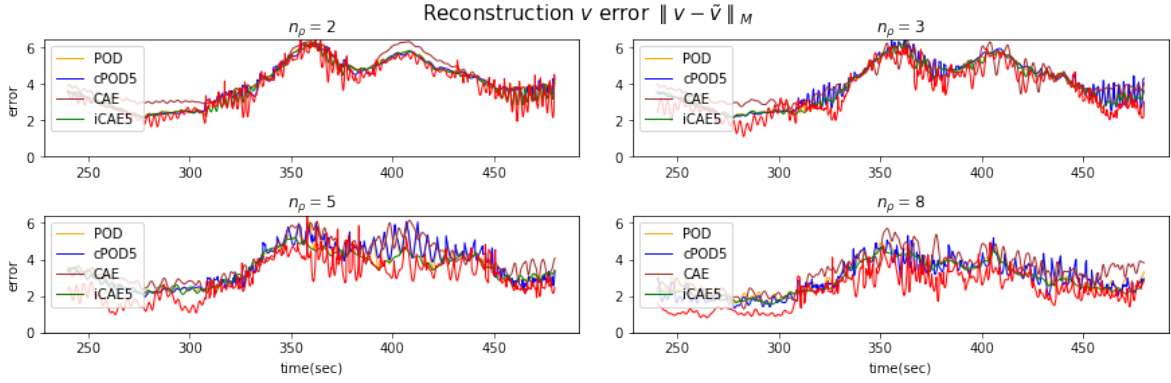
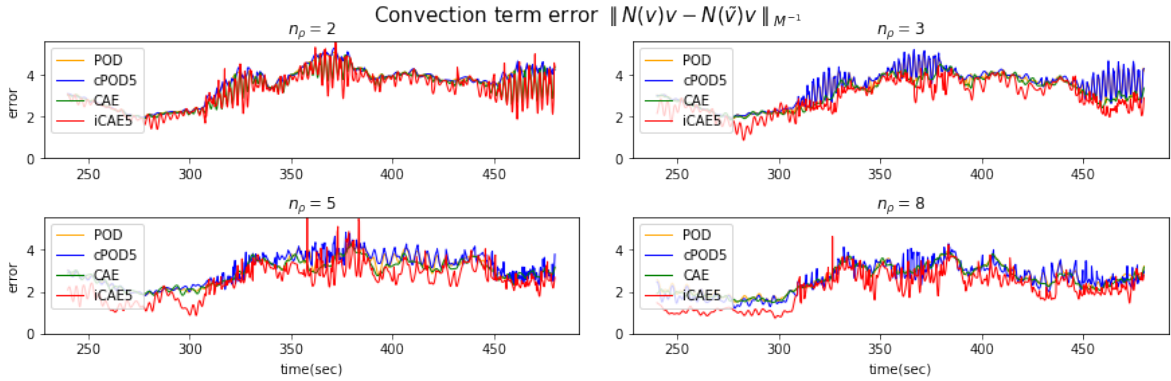
interpolations operations. Hence, we optimize \mathbf{I}_p in the last layer of the decoder and other decoder parameters simultaneously, instead of the usage of the fixed \mathbf{I}_p obtained by the optimization of $\mathbf{v} \approx \mathbf{I}_p \mathbf{v}_{\text{CNN}}$.

Figure 3 shows how the cPOD and the iCAE can improve the reconstruction performance of the standard POD and the CAE respectively. The CNN model and POD have similar results. In very low-dimensional cases ($n_\rho = 2, 3$), the CAE outperforms the cPOD. Regarding the convection term errors, a similar trend to the projection errors is observed except for the cPOD. The error graph of the cPOD increases at $n_\rho = 12$, contrasting with trends that decrease by getting larger n_ρ . Figure 4 shows that the POD and the cPOD suffer from the large performance degradation when $n_\rho = 2$. Taken overall, the iCAE is the best over time. However, peaks occur at around 4 seconds when $n_\rho = 5$.

Figure 5 indicates that the $\mathbf{N}(\mathbf{v})\mathbf{v}$ errors tend to be similar to the reconstruction \mathbf{v} errors and that the pretrained models can approximate $\mathbf{N}(\mathbf{v})\mathbf{v}$ equally well, although the actual convection loss $L = \sum_{i=1}^T \|\mathbf{N}(\mathbf{v}_i)\mathbf{v}_i - \mathbf{N}(\tilde{\mathbf{v}}_i)\mathbf{v}_i\|_{M^{-1}}$ is not used in the training session.

Generally, we observed that the consideration of the FEM norms, e.g., for computing the loss as $L = \sum_{i=1}^T \|\mathbf{v}_i - \tilde{\mathbf{v}}_i\|_2^2$ did not lead to better reconstruction errors while causing a significant computational overhead. Therefore, we stuck to the standard *mean squared error* loss function, that corresponds to the unweighted 2-norm of the vectors representing the states \mathbf{v} and the forms like $\mathbf{N}(\mathbf{v})$.

For the iCAE approach, a classification strategy for the velocity states is learned, once the encoder μ is available. Figure 6 shows that the iCAE5 can capture the periodic flow pattern which is the wake behind a cylinder four seconds later. Literally, data are the most important factor to build data-driven models. In other words, clustering affects reconstruction performance since decoders are trained using clustered datasets. When the states are misclassified, it could cause momentarily sparks that have high errors. According to Figure 4, contrary to the overall performance of the iCAE, several abnormal

Figure 9: Reconstruction error in $[240, 480]$ (Section 5.2).Figure 10: Averaged convection error in $[240, 480]$ for the double cylinder case (Section 5.2).

values are observed in the time period $[4, 5]$ when $n_\rho = 5$.

Next, we use the residual metrics to compare the residuals without resorting to the time derivatives. As mentioned in Section 4, the clustering models cannot reproduce $\hat{\mathbf{v}}$. Moreover, as the computation of the data is based on a sophisticated second order time integration scheme, the error of the numerical evaluation of \dot{v} only based on the snapshots that only roughly covers the time domain totally dominated the residuals. In Figure 7, the errors have a similar trend to the reconstruction errors shown in Figure 3 with iCAE performing best and the linear reconstruction by CAE outperforming POD at the smaller dimensions of ρ . Also not the trajectory plots of the residuals in Figure 4 and Figure 5, that clearly show these trends except from the initial phase where all methods deliver similar approximation results.

5.2 Double Cylinder

As a second example that features richer dynamics, we consider an FEM simulation of Equation (1) for a double cylinder wake with a Reynolds number of 50; see Figure 2 for an illustration of the setup. Here, the state vectors $\mathbf{v}(t) \in \mathbb{R}^{25982}$ (i.e., $n_v = 25982$) are distributed over the physical domain $(-20, 70) \times (-20, 20)$. Accordingly, to obtain the CNN input data $\mathbf{v}_{\text{CNN}}(t) \in \mathbb{R}^{2 \times 47 \times 63}$, an interpolation matrix $\mathbf{I}_c \in \mathbb{R}^{25982 \times (47 \cdot 63)}$ is applied.

For training the models, we use 800 snapshots of x and y directional velocities in the time interval

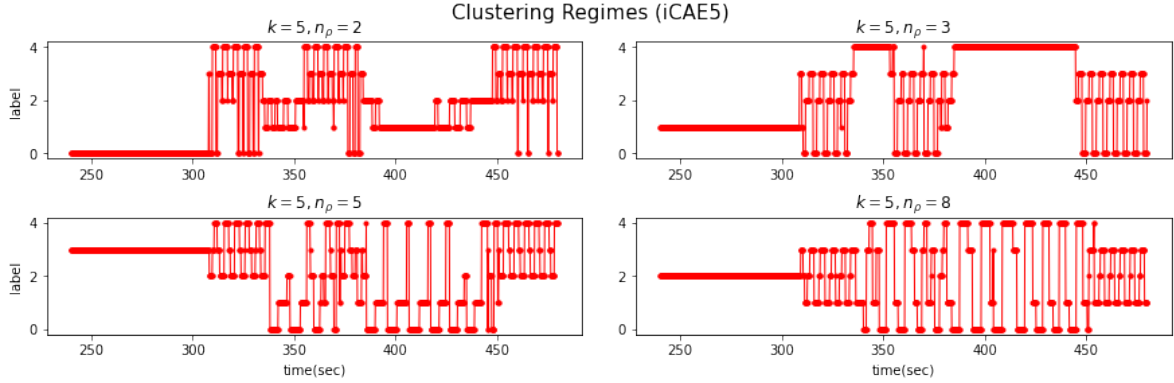


Figure 11: Prompt clustering reaction in [240, 480] for the double cylinder case (Section 5.2).

[240, 480], thus leaving aside the startup phase.

In the evaluation session, 1600 snapshots following the same condition as the training dataset in [240, 480] are used. The rest of the experimental setting is the same as that of the single cylinder case. As a noncompetitive model, we exclude the CNN model (3) from the experiment and then the existing models with the same hyperparameters are applied for the double-cylinder case.

The averaged errors (see Figure 8) confirm the findings of the previous example namely that the iCAE achieve the best results and that the CAE outperforms POD in particular at low parameter dimensions. However, other than for the single cylinder case, a clear gap between the approaches in Figure 9 and Figure 10 displaying the errors over time is not observed. This might be due in particular to the many different regimes of the flow that also appears to be the cause that the clustering results do not show clear patterns if compared against various dimensions of ρ ; see Figure 11 where the iCAE5 yields different clustering outcomes depending on $n_\rho = 2, 3, 5, 8$. Nonetheless, as shown in Figure 12, the iCAE also achieves the lowest error in the residuals of $\Pi^\top(\mathbf{N}(\mathbf{v})\mathbf{v} + \mathbf{A}\mathbf{v})$ over the reduced dimensions n_ρ .

6 Conclusion

In this paper, we have investigated several combinations of POD, convolutional autoencoders, and clustering for low-dimensional parametrizations of fluid flow. We confirmed that, as suggested by numerous theoretical and numerical studies, that the nonlinear approaches can outperform linear methods like POD at the very low dimensions of the parametrization.

Furthermore, we confirmed that neural networks provide a general method for finding these low-dimensional parametrization even in the high-dimensional data regime, in particular if one can exploit sparsity patterns as they are implicitly contained in convolutional neural networks.

In order to probe the limits of the parametrization, we have included k -means clustering on the reduced coordinates so that the reconstruction can be made specific to specific flow regimes. Although this approach (in terms of the iCAE method in this paper) reaches significantly lower error levels in particular at low dimensions, its practical use, e.g., in simulations, is in question because of the nonsmooth operations for the decoding.

In the future, we will investigate the performance of the proposed low-dimensional parametrizations in simulations and controller design. Another relevant future development will concern relaxations of the clustering maps so that reconstruction based on clustering information will become a smooth and possibly even linear operation.

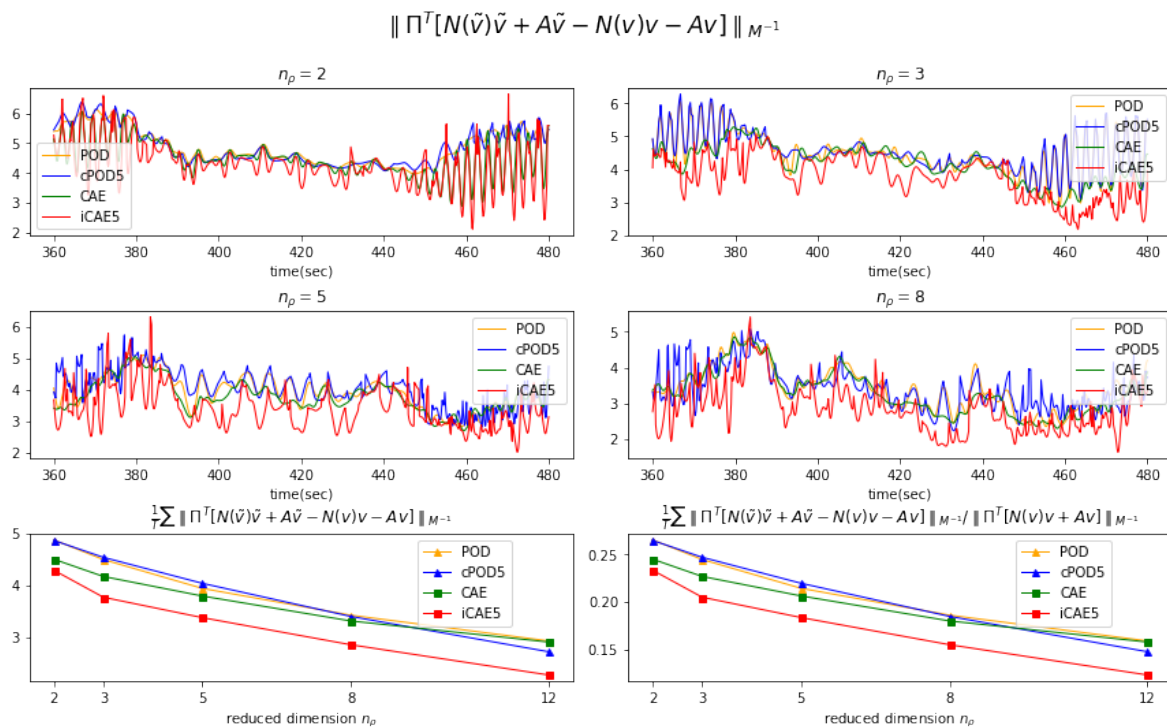


Figure 12: Error of $\Pi^T(\mathbf{N}(\mathbf{v})\mathbf{v} + \mathbf{A}\mathbf{v} - \mathbf{f})$ in $[360, 480]$ (Section 5.2).

7 Code Availability

The source code of the implementations used to compute the presented results is available from [doi:10.5281/zenodo.7575808](https://doi.org/10.5281/zenodo.7575808) under the Creative Commons Attribution 4.0 international license and is authored by Yongho Kim.

Acknowledgments

We acknowledge funding by the German Research Foundation (DFG) through the research training group 2297 “MathCoRe”, Magdeburg.

References

- [1] R. Altmann and J. Heiland. Finite element decomposition and minimal extension for flow equations. *ESAIM Math. Model. Numer. Anal.*, 49(5):1489–1509, September 2015. doi:10.1051/m2an/2015029.
- [2] M. Balcan and K. Q. Weinberger, editors. *Unsupervised Deep Embedding for Clustering Analysis*, volume 48 of *JMLR Workshop and Conference Proceedings*. JMLR.org, 2016. URL: <http://proceedings.mlr.press/v48/xieb16.html>.
- [3] D. Bank, N. Koenigstein, and R. Giryes. Autoencoders. *arXiv*, 2020. URL: <https://arxiv.org/abs/2003.05991>.
- [4] M. Behr, P. Benner, and J. Heiland. Example setups of Navier-Stokes equations with control and observation: Spatial discretization and representation via linear-quadratic matrix coefficients. *ArXiv*, 2017. URL: <https://arxiv.org/abs/1707.08711>.
- [5] G. Berkooz, P. Holmes, and J. L. Lumley. The proper orthogonal decomposition in the analysis of turbulent flows. *Annu. Rev. Fluid Mech.*, 25(1):539–575, 1993. doi:10.1146/annurev.fl.25.010193.002543.
- [6] D.-A. Clevert, T. Unterthiner, and S. Hochreiter. Fast and accurate deep network learning by exponential linear units (ELUs). *ICLR 2016 (Poster)*, 2016. URL: <https://arxiv.org/pdf/1511.07289.pdf>.
- [7] M. M. Fard, T. Thonet, and É. Gaussier. Deep k -means: Jointly clustering with k -means and learning representations. *Pattern Recognit. Lett.*, 138:185–192, 2020. doi:10.1016/j.patrec.2020.07.028.
- [8] S. Fresca and A. Manzoni. POD-DL-ROM: Enhancing deep learning-based reduced order models for nonlinear parametrized PDEs by proper orthogonal decomposition. *Comput. Methods Appl. Mech. Engrg.*, 388:114181, 2022. doi:10.1016/j.cma.2021.114181.
- [9] H. Gao, L. Sun, and J. Wang. PhyGeoNet: Physics-informed geometry-adaptive convolutional neural networks for solving parameterized steady-state PDEs on irregular domain. *J. Comput. Phys.*, 428:110079, 2021. doi:10.1016/j.jcp.2020.110079.
- [10] J. Gao and J. Zhang. Clustered SVD strategies in latent semantic indexing. *Inf. Process. Manag.*, 41(5), 2005. doi:10.1016/j.ipm.2004.10.005.
- [11] I. J. Goodfellow, Y. Bengio, and A. Courville. *Deep Learning*. MIT Press, Cambridge, MA, USA, 2016. URL: <http://www.deeplearningbook.org>.
- [12] J. Heiland, P. Benner, and R. Bahmani. Convolutional neural networks for very low-dimensional LPV approximations of incompressible Navier-Stokes equations. *Frontiers Appl. Math. Stat.*, 8:879140, 2022. doi:10.3389/fams.2022.879140.
- [13] J. Heiland and Y. Kim. Convolutional autoencoders and clustering for low-dimensional parametrization of incompressible flows. *IFAC-PapersOnLine*, 55(30):430–435, 2022. Proceedings of the 25th International Symposium on MTNS. doi:10.1016/j.ifacol.2022.11.091.
- [14] Y. Kim and Y. Choi. Learning finite difference methods for reaction-diffusion type equations with FCNN. *Comput. Math. with*, 123:115–122, 2022. doi:10.1016/j.camwa.2022.08.006.
- [15] D. P. Kingma and J. Ba. Adam: A method for stochastic optimization. *ICLR 2015, Conference Track Proceedings*, 2015. URL: <http://arxiv.org/abs/1412.6980>.

-
- [16] P. J. W. Koelewijn and R. Tóth. Scheduling dimension reduction of LPV models - A deep neural network approach. *Proceedings of the IEEE*, pages 1111–1117, 2020. doi:[10.23919/ACC45564.2020.9147310](https://doi.org/10.23919/ACC45564.2020.9147310).
- [17] Y. Lecun, L. Bottou, Y. Bengio, and P. Haffner. Gradient-based learning applied to document recognition. *Proceedings of the IEEE*, 86(11):2278–2324, 1998. doi:[10.1109/5.726791](https://doi.org/10.1109/5.726791).
- [18] K. Lee and K. T. Carlberg. Model reduction of dynamical systems on nonlinear manifolds using deep convolutional autoencoders. *J. Comput. Phys.*, 404, 2020. doi:[10.1016/j.jcp.2019.108973](https://doi.org/10.1016/j.jcp.2019.108973).
- [19] D. Liu, S. Xie, Y. Li, D. Zhao, and E. M. El-Alfy, editors. *Deep Clustering with Convolutional Autoencoders*, volume 10635 of *Lecture Notes in Comput. Sci.* Springer, 2017. doi:[10.1007/978-3-319-70096-0_39](https://doi.org/10.1007/978-3-319-70096-0_39).
- [20] M. Ohlberger and S. Rave. Reduced basis methods: Success, limitations and future challenges. *Proceedings of the Conference Algorithm*, pages 1–12, 2016. URL: <https://arxiv.org/abs/1511.02021>.
- [21] S. Z. Rizvi, F. Abbasi, and J. M. Velni. Model reduction in linear parameter-varying models using autoencoder neural networks. *IEEE*, pages 6415–6420, 2018. doi:[10.23919/ACC.2018.8431912](https://doi.org/10.23919/ACC.2018.8431912).
- [22] A. Saxena, M. Prasad, A. Gupta, N. Bharill, O. P. Patel, A. Tiwari, M. J. Er, W. Ding, and C. Lin. A review of clustering techniques and developments. *Neurocomputing*, 267:664–681, 2017. doi:[10.1016/j.neucom.2017.06.053](https://doi.org/10.1016/j.neucom.2017.06.053).
- [23] D. Sculley. Web-scale k-means clustering. *WWW'10*, pages 1177–1178, 2010. doi:[10.1145/1772690.1772862](https://doi.org/10.1145/1772690.1772862).
- [24] N. Winovich, K. Ramani, and G. Lin. ConvPDE-UQ: Convolutional neural networks with quantified uncertainty for heterogeneous elliptic partial differential equations on varied domains. *J. Comput. Phys.*, 394:263–279, 2019. doi:[10.1016/j.jcp.2019.05.026](https://doi.org/10.1016/j.jcp.2019.05.026).